Blind Poissonian images deconvolution with framelet regularization

Houzhang Fang, Luxin Yan,* Hai Liu, and Yi Chang

Science and Technology on Multi-spectral Information Processing Laboratory, Institute for Pattern Recognition and Artificial Intelligence, Huazhong University of Science and Technology, Wuhan, Hubei 430074, China
**Corresponding author: yanluxin@gmail.com*

Received December 4, 2012; revised January 2, 2013; accepted January 2, 2013;
posted January 4, 2013 (Doc. ID 181173); published February 6, 2013

We propose a maximum a posteriori blind Poissonian images deconvolution approach with framelet regularization for the image and total variation (TV) regularization for the point spread function. Compared with the TV based methods, our algorithm not only suppresses noise effectively but also recovers edges and detailed information. Moreover, the split Bregman method is exploited to solve the resulting minimization problem. Comparative results on both simulated and real images are reported. © 2013 Optical Society of America

OCIS codes: 100.1455, 100.1830, 100.3020, 100.2000.

In recent years, blind Poissonian images deconvolution methods have received significant attention due to their wide application in microscopy, medical, and astronomical imaging (see [1] for a review and [2–4]). Formally, the blurred noisy image $\mathbf{g} \in \mathbb{R}^N$ (N is the number of pixels of the image.) can be represented in two equivalent matrix-vector notation forms

$$\mathbf{g} = \mathcal{P}(\mathbf{Hu}) = \mathcal{P}(\mathbf{Uh}), \tag{1}$$

where $\mathbf{H} \in \mathbb{R}^{N\times N}$ denotes the matrix notation of the convolution of the point spread function (PSF) $\mathbf{h} \in \mathbb{R}^N$ and $\mathbf{U} \in \mathbb{R}^{N\times N}$ denotes the matrix formed from the latent image $\mathbf{u} \in \mathbb{R}^N$. $\mathcal{P}$ denotes the Poisson noise process. The purpose of blind image deconvolution (BID) is to seek the best estimations of $\mathbf{u}$ and $\mathbf{h}$ from the degraded image $\mathbf{g}$. However, owing to the ill-posed nature of BID, regularization is necessarily introduced in order to enforce stability, as well as incorporate prior knowledge about the solution [5]. In the existing regularization methods, the total variation (TV) [6] and wavelet frames [7] are two widely adopted regularizers for image restoration. However, the TV model favors a piecewise constant solution, which leads to the staircase effect. In previous work [4], we proposed the spatially adaptive TV (SATV) model using the edge indicator to distinguish edges from flat areas in order to reduce the noise in flat regions as well as preserve edge and detailed information. Nevertheless, undersignificant noise and heavy blur, the performances of the SATV and TV are similar. To alleviate the staircase effect, some high order differential operators [8] were proposed to replace the first-order gradient operator in the TV model. Recently, framelet regularization has been introduced in motion deblurring [7], which assumes that natural images have sparse approximation under the framelet transform. Since framelet transform has the ability of multiple-resolution analysis in nature, different framelet masks reflect different orders of difference operators, which can adaptively capture multiscale edge structures in an image. Therefore, it can well preserve various types of edges simultaneously. It motivates us to apply framelet regularization in blind Poissonian images deconvolution. The proposed method can preserve different scale structure information of the images and produce a smoother solution. Moreover, it can efficiently suppress noise.

Considering the cases where the data is contaminated by Poisson noise, the intensity of each pixel $\mathbf{g}_i$ in the observed image is a random variable that follows an independent Poisson distribution. Hence the likelihood can be written as

$$p(\mathbf{g}|\mathbf{u},\mathbf{h}) = \prod_{i=1}^{N} \frac{(\mathbf{Hu})_i^{\mathbf{g}_i}\ \exp\left(-\mathbf{Hu}\right)_i}{\mathbf{g}_i!}. \tag{2}$$

In the Bayesian framework, we model the framelet based sparsity prior model $p(\mathbf{u})$ on the object $\mathbf{u}$ and the TV sparsity prior model $p(\mathbf{h})$ on the PSF as

$$p(\mathbf{u}) \propto \exp(-\tau\|\mathbf{Wu}\|_1), \qquad p(\mathbf{h}) \propto \exp(-\alpha\|\nabla\mathbf{h}\|_1), \tag{3}$$

where $\mathbf{W}$ denotes the framelet transform, τ and α are the positive parameters. According to the Bayes rule, the a posteriori density is $p(\mathbf{u},\mathbf{h}|\mathbf{g}) \propto p(\mathbf{g}|\mathbf{u},\mathbf{h})p(\mathbf{u})p(\mathbf{h})$, the maximum a posteriori estimation is then equivalent to minimizing the functional $E(\mathbf{u},\mathbf{h}) = -\log p(\mathbf{u},\mathbf{h}|\mathbf{g})$, i.e., to minimize

$$E(\mathbf{u},\mathbf{h}) = \sum_{i=1}^{N}[(\mathbf{Hu})_i - \mathbf{g}_i\ \log\left(\mathbf{Hu}\right)_i] + \tau\|\mathbf{Wu}\|_1 + \alpha\|\nabla\mathbf{h}\|_1 + l_{\mathbf{u}\geq 0}, \tag{4}$$

here, the role of $l_{\mathbf{u}\geq 0}$ is to impose the non-negative constraint on the estimation image $\mathbf{u}$.

Thus, our method is to seek the optimal $\mathbf{u}$ and $\mathbf{h}$ that minimize $E(\mathbf{u},\mathbf{h})$. The functional (4) is intuitive, it penalizes the ℓ_1-norm of the framelet transform coefficients of the image $\mathbf{u}$ and imposes the non-negativity constraint on the image, and enforces a TV constraint on the PSF aiming to increase the robustness to noise. The alternate minimization approach [6,7] can be applied to find $\mathbf{u}$ and $\mathbf{h}$: in each step of the iterative procedure we minimize with respect to either $\mathbf{h}$ or $\mathbf{u}$ while keeping the other one fixed. The update of the PSF $\mathbf{h}$ can be written as [2]

 © 2013 Optical Society of America

$$\mathbf{h}_t^{k+1} = \frac{\mathbf{h}^k}{1-\alpha\,\mathrm{div}\left(\frac{\nabla\mathbf{h}^k}{|\nabla\mathbf{h}^k|}\right)}\left\{(\mathbf{U}^k)^T\left[\frac{\mathbf{g}}{\mathbf{U}^k\mathbf{h}^k}\right]\right\},$$
$$\mathbf{h}^{k+1} = \frac{\mathbf{h}_t^{k+1}}{\sum_{i=1}^{N}(\mathbf{h}_t^{k+1})_i}, \tag{5}$$

where the superscript T denotes the adjoint operation. The difficulties in finding $\mathbf{u}$ are that the data term is nonquadratic and nonseparable and the ℓ_1-norm term $\|\mathbf{Wu}\|_1$ is nonsmooth and nonseparable. To overcome these, we use split Bregman method [9]. The idea is to convert the unconstrained minimization problem on $\mathbf{u}$ in (4) into a constrained one by introducing three auxiliary variables $\mathbf{d}_1 = \mathbf{Hu}$, $\mathbf{d}_2 = \mathbf{Wu}$, and $\mathbf{d}_3 = \mathbf{u}$. Further the problem can be converted into an unconstrained problem via the Bregman iteration:

$$\min_{\mathbf{u},\mathbf{d}_1,\mathbf{d}_2,\mathbf{d}_3}\sum_{i=1}^{N}[(\mathbf{d}_1)_i - \mathbf{g}_i\log(\mathbf{d}_1)_i] + \tau\|\mathbf{d}_2\|_1 + l_{\mathbf{d}_3\ge 0}(\mathbf{d}_3)$$
$$+\frac{1}{2\gamma}(\|\mathbf{d}_1-\mathbf{Hu}-b_1\|_2^2 + \|\mathbf{d}_2-\mathbf{Wu}-\mathbf{b}_2\|_2^2$$
$$+\|\mathbf{d}_3-\mathbf{u}-\mathbf{b}_3\|_2^2), \tag{6}$$

where γ is the penalty parameter. Clearly, the minimizations of (6) with respect to $\mathbf{u}$, $\mathbf{d}_1$, $\mathbf{d}_2$, and $\mathbf{d}_3$ are decoupled, thus, can be further converted into four separate subminimization problems where the update formulas respectively are then

$$\mathbf{u}^{k+1} = \frac{\mathbf{H}^T(\mathbf{d}_1^k - b_1^k) + \mathbf{W}^T(\mathbf{d}_2^k - \mathbf{b}_2^k) + \mathbf{d}_3^k - \mathbf{b}_3^k}{\mathbf{H}^T\mathbf{H} + 2\mathbf{I}}, \tag{7}$$

$$\begin{cases}\mathbf{d}_1^{k+1} = \frac{1}{2}\left(s^k + \sqrt{(s^k)^2 + 4\gamma\mathbf{g}}\right),\\ \mathbf{d}_2^{k+1} = \max\{\|\mathbf{Wu}^{k+1} + \mathbf{b}_2^k\|_1 - \tau\gamma, 0\}\frac{\mathbf{Wu}^{k+1}+\mathbf{b}_2^k}{\|\mathbf{Wu}^{k+1}+\mathbf{b}_2^k\|_1},\\ \mathbf{d}_3^{k+1} = \max\{\mathbf{u}^{k+1} + \mathbf{b}_3^k, 0\},\end{cases} \tag{8}$$

where $s^k = \mathbf{b}_1^k + \mathbf{Hu}^{k+1} - \gamma$, $\mathbf{I}$ is the identity matrix. $\mathbf{b}_1$, $\mathbf{b}_2$, and $\mathbf{b}_3$ are the Bregman variables and are updated as follows:

$$\begin{cases}\mathbf{b}_1^{k+1} = \mathbf{b}_1^k + \mathbf{Hu}^{k+1} - \mathbf{d}_1^{k+1},\\ \mathbf{b}_2^{k+1} = \mathbf{b}_2^k + \mathbf{Wu}^{k+1} - \mathbf{d}_2^{k+1},\\ \mathbf{b}_3^{k+1} = \mathbf{b}_3^k + \mathbf{u}^{k+1} - \mathbf{d}_3^{k+1}.\end{cases} \tag{9}$$

In (7), we set $\mathbf{d}_1^0 = \mathbf{d}_2^0 = \mathbf{d}_3^0 = \mathbf{b}_1^0 = \mathbf{b}_2^0 = \mathbf{b}_3^0 = 0$, $\mathbf{H}$ is the block-circulant with circulant-block matrix. Thus, (7) can be well implemented using the fast Fourier transform to reduce the computational burden. Once $\mathbf{u}^{k+1}$ is obtained, the three equations in (8) can be computed parallelly. Subsequently, the three equations in (9) can be also calculated parallelly. The B-splines framelet [7] is used in our implementation. The interested reader can refer to [7,10] for more implementation details on the framelet transform.

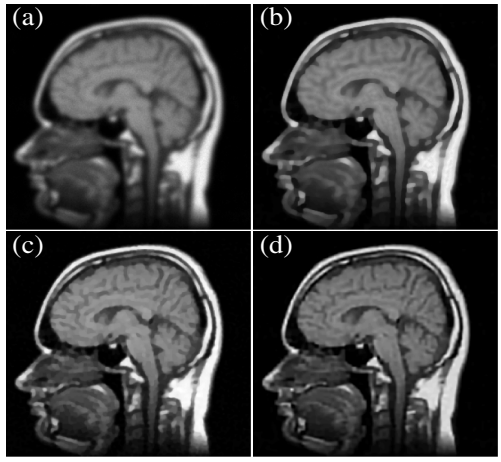


Fig. 1. Restoration of a simulated degraded image. (a) Degraded image, image restoration by (b) RLTV, (c) RLSATV, and (d) BPIDFR.

To test the performance of the proposed method (BPIDFR), we executed simulations with three kinds of images (because of page limitation, test images are omitted here) under Poisson noise process. Specifically, owing to the statistical error of low photon counts, the medical, microscopical, and astronomical images are typically corrupted by Poisson noise. Each image is degraded by the 15×15 Gaussian blur kernel with the standard deviation of 2.5. Then the resulting blurred image was contaminated by Poisson noise. For comparison, the Richardson–Lucy total variation (RLTV) [2] and RLSATV [4] blind deconvolution algorithms were also tested. To measure the improvement in the restored image quality, the normalized mean square error (NMSE) $\|\mathbf{u}-\hat{\mathbf{u}}\|_2^2/\|\mathbf{u}\|_2^2$ is used, where $\mathbf{u}$ and $\hat{\mathbf{u}}$ are the original and the restored image, respectively.

First, we consider the medical image. Figure 1 shows a computed tomography brain images simulation example of restoration by RLTV, RLSATV, and BPIDFR. In our test, we use the following setting: $\tau = 0.002$, $\gamma = 20/\tau$, $\alpha = 0.0008$, and 200 iterations. Comparing Fig. 1(c) with Fig. 1(d), it is observed that BPIDFR is able to preserve images details and suppress Poisson noise simultaneously. The NMSE of three kinds of the degraded images and the best restored images by the three methods are compared in Table 1. The best restored image is selected to be the one with the lowest NMSE when the regularization parameter changes. It can be seen that the BPIDFR has achieved the smallest NMSE among the three methods, and NMSE of the BPIDFR method is considerably smaller than that of the degraded image for

Table 1. NMSE of Degraded Image and the Best Restored Image (with the Lowest NSME) by Different Algorithms

		Image Restoration by		
Image	Degraded Image	RLTV	RLSATV	BPIDFR
Brain	0.0567	0.0293	0.0198	0.0166
Circuit	0.0268	0.0125	0.0095	0.0079
Satellite	0.0741	0.0500	0.0431	0.0393

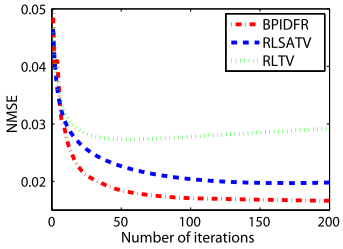


Fig. 2. (Color online) NMSE versus the iteration number of the three methods for the brain image.

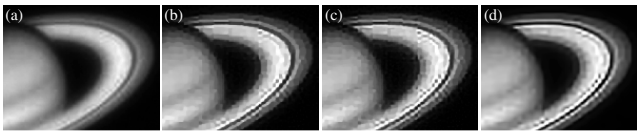


Fig. 3. Restoration of a Saturn image [11]. (a) Degraded image, image restoration by (b) RLTV, (c) RLSATV, and (d) BPIDFR.

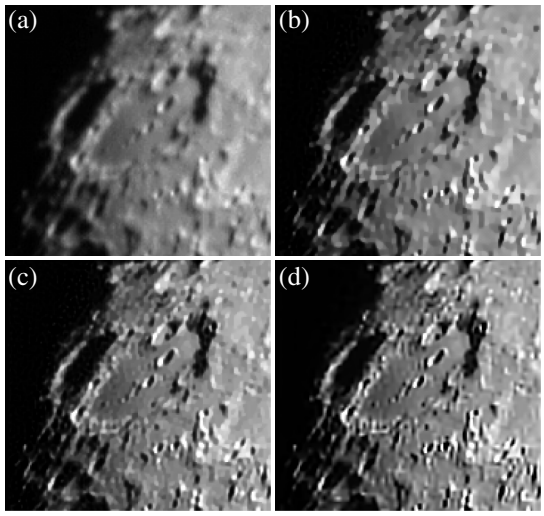


Fig. 4. Restoration of a lunar soil image [12]. (a) Degraded image, restoration by (b) RLTV, (c) RLSATV, and (d) BPIDFR.

every image. The NMSE versus the number of iterations of the three methods on the brain image are plotted in Fig. 2, where the convergence of BPIDFR is also highlighted.

We further show the ability of our approach on real astronomical images. An example of a real degraded Saturn image is shown in Fig. 3. We use $\tau = 0.001$, $\gamma = 10/\tau$, and $\alpha = 0.0008$, starting with 25×25 Gaussian kernel with the started deviation of 1.5 for the initial PSF and 180 iterations. Figure 3(b) is the restored result by RLTV, noticeable piecewise constant can be seen. Although RLSATV can restore more details compared with RLTV as shown in Fig. 3(c), it also obviously introduces artifacts caused by noise. BPIDFR remarkably reduces these adverse effects and as shown in Fig. 3(d), it looks sharper as well as the edges are better preserved.

Another example of a real degraded lunar soil image is shown in Fig. 4. We set $\tau = 0.001$, $\gamma = 2/\tau$, and $\alpha = 0.0008$ and choose 15×15 Gaussian kernel with the started deviation of 1.8 as the initial PSF and 200 iterations. It can be observed from Figs. 4(b) and 4(c) that the recovered images by RLTV and RLSATV still exist piecewise constant effects. Also, the noise amplification are apparent, especially around the limb background of the moon. The improvement of the RLSATV method is not notable because the image contains little large scale structure information. As shown in Fig. 4(d), the restored image by BPIDFR looks natural with much richer detail information, such as the craters of the moon surface. This happens because of the framelet regularization. Since different framelet masks reflect different orders of difference operators, BPIDFR can adaptively apply difference operators according to the singularities of the underlying solutions. Therefore, it can well preserve various types of edges simultaneously. In addition, the framelet coefficients of the noise pixels are large, which are significantly penalized by the regularization term $\|\mathbf{Wu}\|_1$. Consequently, the noise is suppressed substantially.

In conclusion, a new blind Poissonian images deconvolution algorithm based on framelet regularization has been introduced. The proposed method exploits the sparsity of the image in the framelet transform domain. Efficient numerical algorithms were also introduced based on the split Bregman algorithm. Comparative results on simulated and real images show that the framelet based method outperforms the TV-based methods in terms of restoring sharp features like edges as well as suppressing the noise.

This work was supported by the Projection of the National Natural Science Foundation of China under Grant 60902060. The authors are grateful to the reviewers for the valuable and insightful suggestions, which have brought great improvements to this manuscript.

References

1. P. Campisi and K. Egiazarian, eds., *Blind Image Deconvolution: Theory and Applications* (CRC, 2007).
2. N. Dey, L. Blanc-Feraud, C. Zimmer, P. Roux, Z. Kam, J. C. Olivo-Marin, and J. Zerubia, Microsc. Res. Tech. **69**, 260 (2006).
3. Z. Xu and E. Y. Lam, Opt. Lett. **34**, 1453 (2009).
4. L. Yan, H. Fang, and S. Zhong, Opt. Lett. **37**, 2778 (2012).
5. D. A. Hope and S. M. Jefferies, Opt. Lett. **36**, 867 (2011).
6. T. F. Chan and C. Wong, IEEE Trans. Image Process. **7**, 370 (1998).
7. J. Cai, H. Ji, C. Liu, and Z. Shen, IEEE Trans. Image Process. **21**, 562 (2012).
8. S. Lefkimmiatis, A. Bourquard, and M. Unser, IEEE Trans. Image Process. **21**, 983 (2012).
9. T. Goldstein and S. Osher, SIAM J. Imaging Sci. **2**, 323 (2009).
10. J. Cai, Framelet toolbox version 2.02, http://www.math.uiowa.edu/~jiancai/code/SplitBreg_Deblur.zip.
11. http://www.cmnh.org/site/AtTheMuseum/PlanetariumandObservatory/AstronomyLectures.aspx.
12. http://www.astrospider.com/images/moon/moon002.jpg.